Journal of Inorganic and Organometallic Polymers and Materials (2022) 32:3725–3737
https://doi.org/10.1007/s10904-022-02363-4

Nanoarchitectonics of Copper Tungsten-Mesoporous Silica with a New Template for Photo Oxidative-Desulfurization of Dibenzothiophene

Heba M. Salem[1] · **Dina Mohmed**[1] · **E. G. Zaki**[1]

Received: 8 March 2022 / Accepted: 27 April 2022 / Published online: 25 May 2022

Abstract

A novel $CuWO_4/SiO_2$ heterojunction catalyst was successfully synthesized using a new sulfonamide derivative. The physical characteristics of the prepared samples were investigated by TGA, XRD, FTIR, SEM, UV, PL, and XPS. The prepared catalysts were applied as a nano photocatalyst for photooxidative desulfurization of dibenzothiophene under visible light using hydrogen peroxide as an oxidant. The photocatalytic oxidative desulfurization performances of the prepared samples were investigated. Various factors as the reaction time, dibenzothiophene concentration, catalyst dose, and the oxidizing agent dose were also studied. The prepared photocatalyst has high desulfurization activity in the removal of DBT under mild conditions. Results showed that the $CuWO_4/SiO_2$ exhibited considerably higher activity than neat support SiO_2. Such improved photocatalytic activity is mainly attributed to the efficient separation of photogenerated electron–hole pairs on $CuWO_4/SiO_2$ heterojunction. Moreover, the synergistic effects of this photocatalytic oxidation and the green oxidant hydrogen peroxide played an essential role in desulfurization. The reaction is pseudo-first-order and can reach 98.6% removal of dibenzothiophene after 70 min and 97.2% after four cycles.

Graphical Abstract

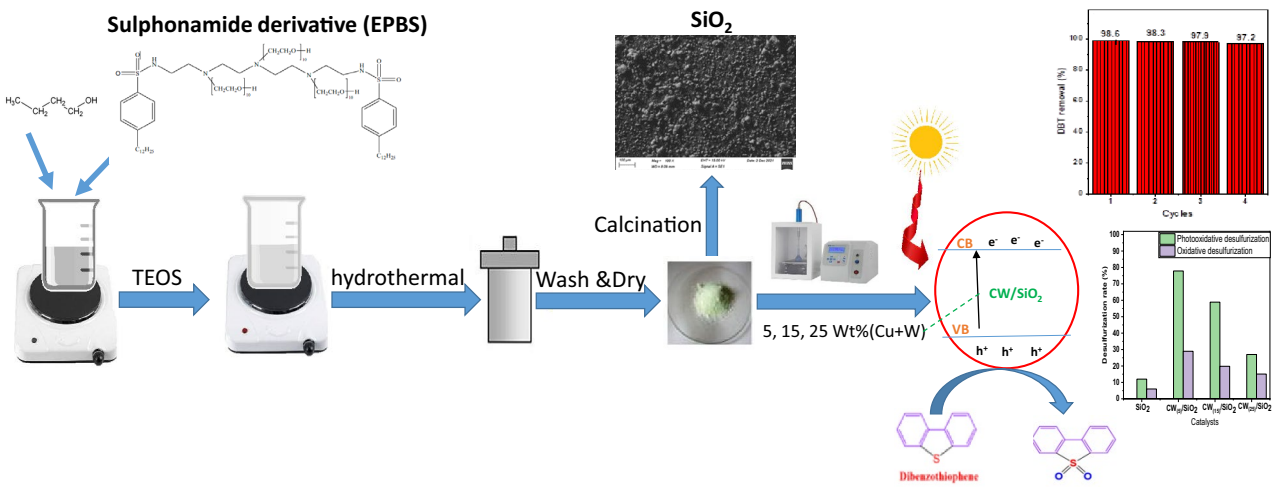

Keywords Photocatalytic oxidative desulfurization · Mesoporous silica · Visible light · Metal oxide catalyst · Dibenzothiophene

✉ Heba M. Salem
hebasalem@epri.sci.eg

Extended author information available on the last page of the article

The chemical structure of synthesized sulfonamide derivative (EPBS).

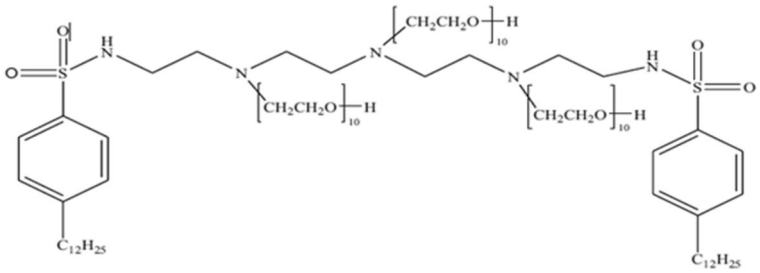

1 Introduction

The desulfurization of transportation fuels has attracted much attention by the researchers because the organosulfur compounds present in crude oil cause a serious problem of pollution in the environment. The sulfur-containing compounds during the combustion process are converted to SO_x compounds, that compounds are the reason of acid rains, soil pollution, air pollution, poisons the catalyst in industry or car exhaust, and corrosion of the refinery equipment [1–4]. So, there are great efforts to restrict the sulfur content in the liquid fuel [5]. The traditional process in the desulfurization of liquid fuel is the hydro-desulfurization process; in this process, a great amount of high cost hydrogen was used, high temperature 300–400 °C and high pressure 3–13 MPa. That process is more effective for the light sulfur compounds such as thiols, sulfides, and thiophenes compounds and their derivatives. But; the more complicated sulfur compounds such as benzothiophene, dibenzothiophene, and their derivatives are very difficult to remove by hydro-treating process [6, 7]. So, there are other techniques had discovered for fuel desulfurization at mild conditions from temperature and pressure and no hydrogen consumption as; biodesulfurization [8], extractive desulfurization [9], adsorptive desulfurization [10, 11], oxidative desulfurization [12, 13] and photooxidation [14, 15].

Photocatalytic oxidative desulfurization is an effective method for oxidizing the sulfur compounds to sulfoxides or sulfones which are more polar and can easily remove by adsorption or solvent extraction. The photocatalytic process depends on using photocatalyst as (ZnO, MO_3, WO_3, TiO_2, $LaVO_4$, CeO_2, etc.,) [16–18] and source of light (visible light or ultraviolet light) [19, 20] to generate energy greater than a bandgap of catalyst to allow charge transfer process. CuO is a monoclinic p-type semiconductor with a band gap of 1.21–1.70 eV [21]. Despite the fact that pure CuO has poor photocatalytic performance due to its low charge transfer rate, prior studies have shown that charge separation and oxygen reduction of photocatalysts created by coupling CuO with other semiconductors has improved [22]. A p-n heterojunction is created when the p-type semiconductor CuO comes into contact with an n-type semiconductor. CuO serves as an electron capture point, preventing electron and hole recombination. As a result, the photocatalytic performance of the p-n heterojunction was enhanced [23]. Despite the high photocatalytic performance of the metal-doped modified p-n heterojunction, it is nevertheless limited by significant agglomeration. Loading on the carrier is one technique to resolve the agglomeration problem. Herein a novel CuO/WO_3 heterojunction photocatalyst was prepared and loaded on SiO_2 and applied in PODS with dibenzothiophene (DBT) as a model sulfur compound CuO/WO_3.

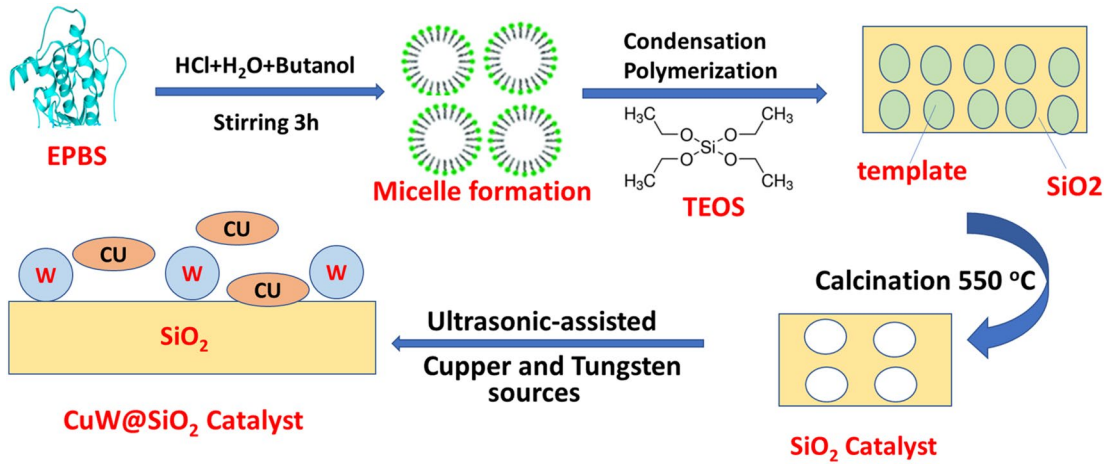

Scheme 1 Photocatalyst synthesis method

The crystallinity, morphology, pore structure, and acidity of the prepared catalyst are affected by the type of template used in the preparation process [24]. Dina et al. prepared mesoporous rod like aluminium oxide using cetyltrimethylammoniumpromide as a template [10]. Ordered mesoporous silica was prepared using nonionic Pluronic P123 by Heba et al. [24]. Akira et al. were prepared the Porous spherical CeO_2 particles using organic monolith particles as a template [25]. In this work we used a template that has abroad applicability, more familiar, and more economical material. We used a sulfonamide derivative EPBS [26] which was prepared previously by shamsel-Din et al. as a template in preparation a mesoporous silica. The ultrasonic-assisted method was used to impregnate Cu and W nanoparticles on the mesoporous silica to improve its photocatalytic performance. The photocatalytic activity of the synthesized photocatalysts were examined using Dibenzothiophene as a sulfur model for contaminants. Furthermore, the efect of several parameters was PODS of dibenzothiophene investigated, including catalyst dose, oxidant dose, Reaction time and recycling times.

2 Experimental

2.1 Materials

Cetyltrimethylammonium bromide (CTAB), tetraethylorthosilicate (TEOS), and Dibenzothiophene (DBT) from Sigma Aldrich, n-octane (95%) from Samchun, Cu nitrate ($CuNO_3$, 99%) from Merck, and Sodium tungstate ($Na_2WO_4{\cdot}2H_2O$) from Panreac Quimica SA were used for sample preparation. H_2O_2 solution (30% w/w aqueous solution) was used as an oxidizing agent.

2.2 Preparation of the Catalyst

2.2.1 Preparation of Mesoporous Silica

The hydrothermal method was used to prepare mesoporous silica using a sulfonamide derivative (EPBS) as a template and tetraethyl orthosilicate (TEOS), n-butanol as a source of silica and co-solvent, respectively. The preparation method was as follows: EPBS dissolved in hydrochloric acid for 3 h under stirring, butanol and deionized water were added into it. The solution was stirred for around 1 h and then dropped TEOS and heated up to 318 K. After 2 days the solution was transferred into a Teflon bottle at 373 K. Filtering, washing, and drying at room temperature were carried out. The dried product was finally calcined at 823 K for 5 h. The TEOS/EPBS/HCl/H_2O/BuOH molar ratio synthesis gel structure is as follows: (2:1:10:10:3).

2.2.2 Preparation of the CW /SiO_2 Nanocomposite

A series of CW/SiO_2 nanocomposites were synthesized via the ultrasonic-assisted method, and the molar ratio of Cu and W was kept the same. Cupper and Ammonium tungstate is used as cupper and tungsten sources. Ammonium tungstate and cu solutions with different concentrations were added to the as-synthesized nano SiO_2 support by the incipient wetness technique. The mixtures were treated with an ultrasonic to disperse Cu and W nanoparticles well and then dried in an oven at 383 K for 12 h. Finally, the samples were calcined at 673 K in open air at 2 °C/min for 4 h. The mass percent of CW in CW/SiO_2 nanocomposite were controlled to be 5, 15, and 25 wt.%, which were designated as $CW_{(X)}/SiO_2$, and the X (X = 5, 15, 25%). The photocatalyst synthesis method is illustrated in Scheme 1.

2.3 Characterization Techniques

The DSC-TGA was measured in an N_2 atmosphere with a heating rate of 10 °C/min using (DSC-TGA SDTQ 600, USA). X-ray diffraction (XRD) patterns were detected using XRD instrument (Germany) version X'Pert Pro outfitted with Ni-filtered Cu-K radiation (λ = 0.1542 nm). Quantachrome Nova 3200 instrument (USA) was used for measuring the surface area and pore volume from the BET plot and BJH equation, respectively, based on the N_2 adsorption–desorption isotherm. Fourier transforms infrared (FTIR) analysis was recorded on a Bruker Tensor 27 infrared spectrometer (Germany). The UV-reflectance analysis was obtained using a JASCO UV spectrophotometer model V-570 (Japan). Photo-luminance (PL) analysis was analyzed at room temperature using the spectrophotometer model JASCO FP-6500-Japan. Surface morphology images were captured using an emission scanning electron microscope (SEM) model Zeiss ULTRA Plus (Germany), in the nanotechnology center, Egyptian petroleum research institute. SEM photographs were collected at 1.5 keV and were then analyzed using Smart SEM. X-ray photoelectron spectroscopy (XPS) data were obtained on K-ALPHA (Thermo Fisher Scientific, USA) with monochromatic X-ray Al K-alpha radiation ranging from 10 to 1350 eV, with a spot size of around 400 m at a pressure of 109 bar, full-spectrum pass energy of 200 eV, and a narrow spectrum pass energy of 50 eV.

2.4 Photocatalytic Oxidative DBT

The reaction was carried out under constant stirring in a 25 mL glass vessel containing 10 mL of n-octane solution and DBT (500 ppm) as a fuel model. The mixture was stirred continuously for 30 min before illumination to attain adsorption–desorption equilibrium between catalyst and DBT in the dark. After that, 30 wt.% H_2O_2 as an oxidant was added to the reaction system followed by irradiation with a linear halogen lamp (visible irradiation has a wavelength of 550 nm). DBT concentration was determined by a UV–visible spectrophotometer, Perkin Elmer model Lambda 25 at 313 nm. In this study, several factors were studied, the effect of the light source, catalyst dose, Oxidant dose, and the reaction time. In terms of catalyst recycling, the solid phase could be recovered by centrifugation after the first reaction, and the solid phase was then dried at 80 °C overnight. Then, fresh H_2O_2 and model oil were added to the reactor for the next run. DBT absorption was measured using a UV–Vis spectrophotometer at $\lambda_{max} = 325$ nm. The high absorbance at 325 nm indicates an n–p* excitation comparable to that of the sulfur atom in DBT [27, 28].

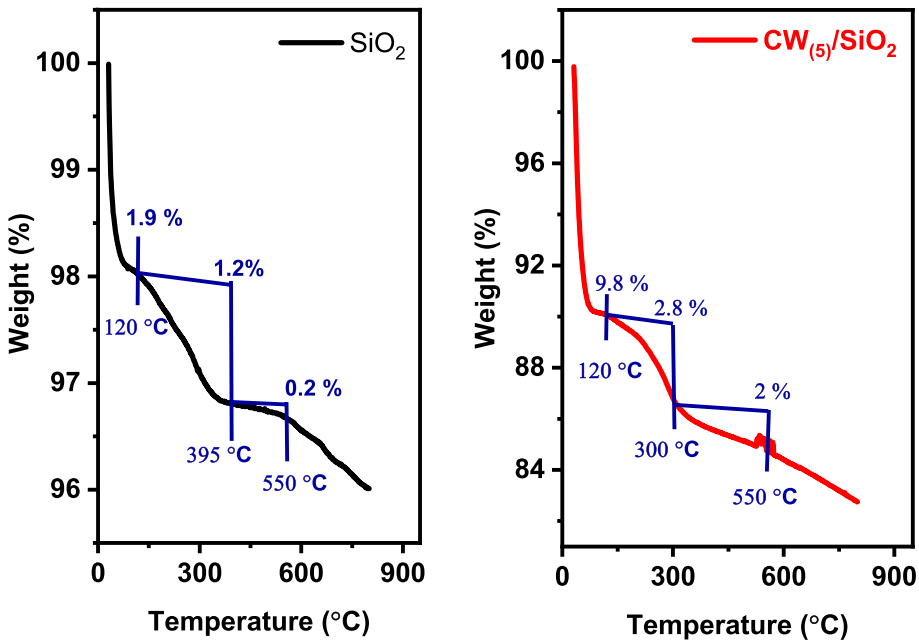

Fig. 1 The thermogravimetric curves of SiO_2 and $CW_{(5)}/SiO_2$

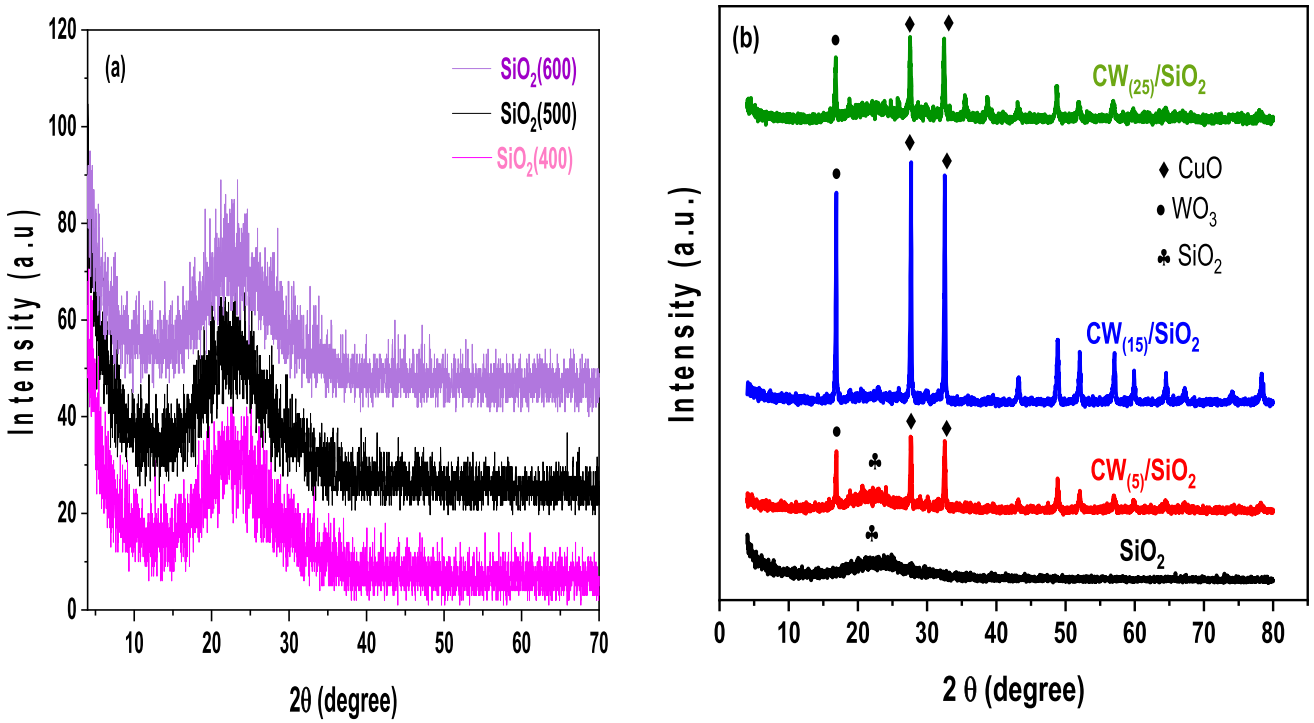

Fig. 2 XRD pattern of silica, **a** at different calcination temperatures (400, 500, and 600 °C) and **b** at different CuW loaded (0, 5, 15, and 25%)

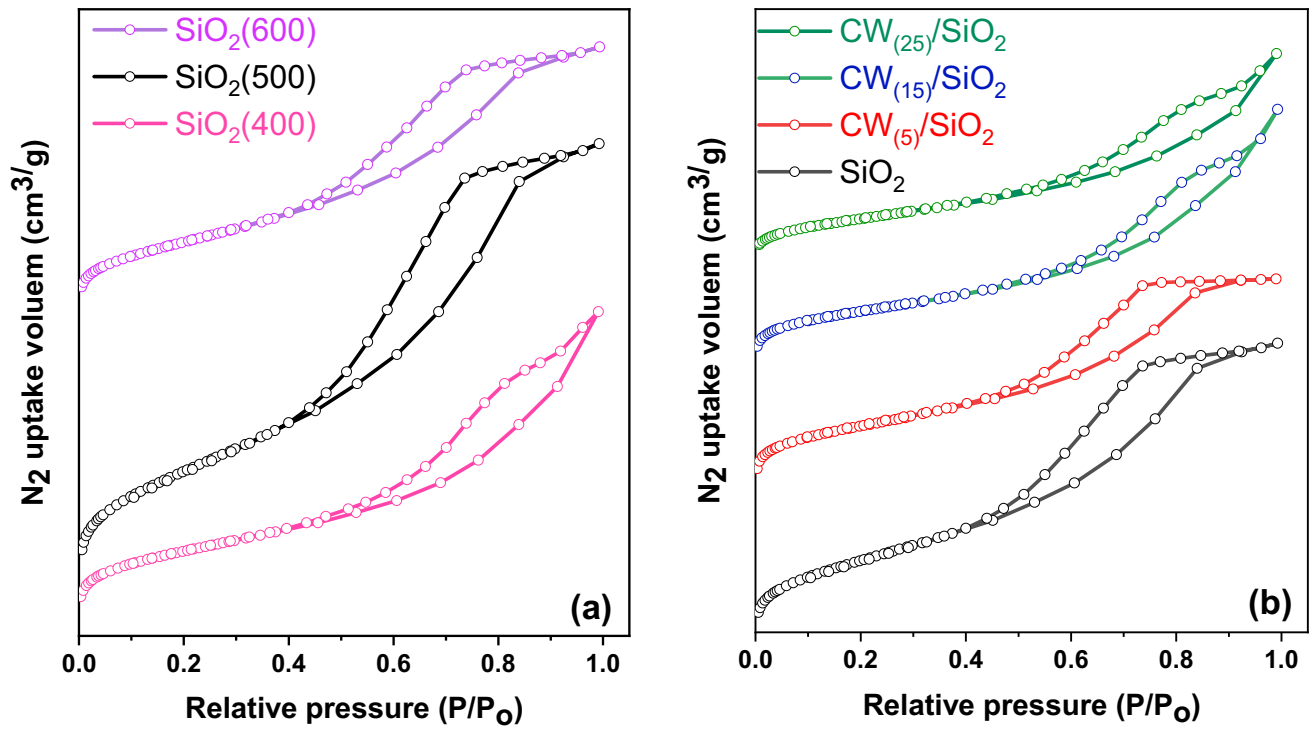

Fig. 3 Nitrogen adsorption–desorption isotherm for the samples calcined at different temperatures and the samples with different percent of impregnated oxides

Table 1 Physico-chemical characteristics of SiO_2 at different calcination temperatures and different loading percentages

Calcination temp. (°C)	BET surface area (m^2/gm)	Total pore volume (cc/gm)	Average pore size (nm)
400	470	0.79	6.8
500	863	1.10	5.4
600	484	0.68	5.6
% of CW			
5	670	0.84	5.1
15	556	1.00	7.1
25	452	0.81	7.2

3 Results and Discussions

3.1 Thermal Gravimetric Analysis

In the thermogravimetric curves Fig. 1a, b there are three actions, the first one at 120 °C due to the loss of adsorbed water and alcohol. The second action of weight loss at 395 °C and 300 °C, may be attributed to the decomposition of organic template sulfonamide. The third event at 550 °C is almost due to the dehydroxylation and loss of the strongly bounded water molecules to the formation SiO_2 and $CW_{(5)}/SiO_2$ as in Fig. 1. In terms of the little overall weight loss seen at the end of the thermal study, SiO_2 and $CW_{(5)}/SiO_2$ nanoparticles show a similar trend and display high thermal stability up to 1000 °C.

3.2 XRD

The X-ray diffraction patterns of the silica at different calcination temperatures (400, 500, and 600 °C) are compared as presented in Fig. 2a. The broad peak at $2\theta = 15–30°$ is evidence of amorphous silica species. The formation of crystalline CuO and WO_3 species were shown in Fig. 2b at samples CW_5/SiO_2, CW_{15}/SiO_2, and CW_{25}/SiO_2. The intensity of the crystallites peaks increased with Cu and W loading but at CW_{25}/SiO_2 the intensity decreased that may be due to the formation of crystalline species inside the pores.

3.3 N_2 Adsorption–Desorption Isotherm

From Fig. 3a all the samples calcined at different temperatures give type IV isotherm characteristics for mesoporous structure materials. But, the materials calcined at 400 °C give H_3 hysteresis loop does not have a plateau at high values of P/P_0 that mean, there is no well-defined mesopore volume [29]. Wheres, the materials calcined at 500 and 600 °C give H_2 hysteresis loop that type of hysteresis indicates the ordered structure of silicate/aluminosilicate pore structures, as the sample $CW_{(5)}/SiO_2$ in Fig. 3b. As shown in Table 1 there is an increase in surface area from 470 to 863 m^2/gm when increasing the calcination temperature from 400 to 500 °C and a decrease in pore size from 6.8 nm to 5.4 nm when increasing the calcination temperature to 500 of that may be due to the formation of new pores with smaller size and larger in numbers. While increasing the calcination temperature to 600 °C there is much decrease in surface area and total pore volume to 484 m^2/gm and 0.68 cm^3/gm respectively. That means the high calcination temperature blocked the pores.

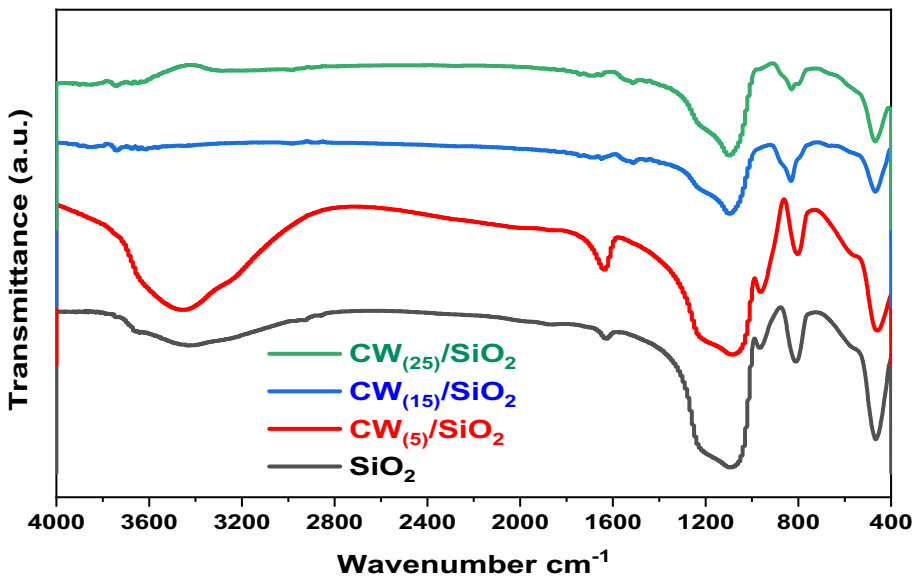

Fig. 4 FTIR of the prepared catalysts

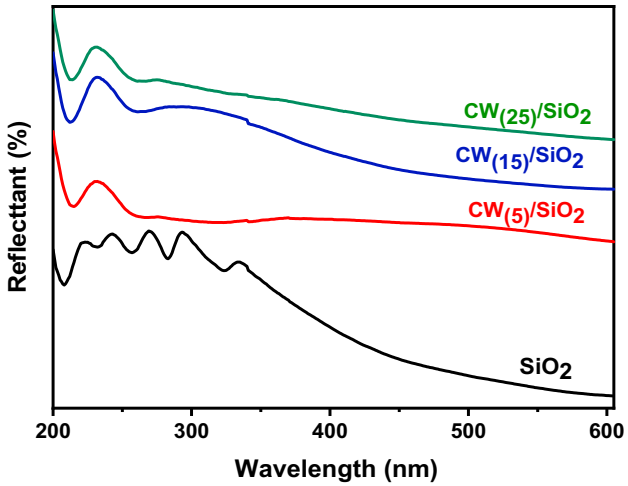

Fig. 5 UV–Visible absorption spectra of impregnated samples

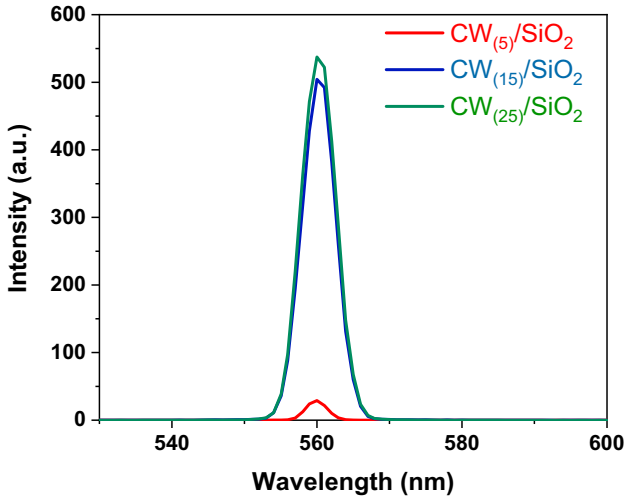

Fig. 6 Photoluminescence of the impregnated samples

When impregnated CuW on silica calcined at 500 °C with different percentages there is a slight decrease in surface area and a little decrease in total pore volume at sample $CW_{(5)}/SiO_2$ which means the most active surface area on the surface. When increasing the percent of impregnated metal to 15 and 25% there is a decrease in surface area and an increase in pore size which means, there are larger pores that may be formed.

3.4 FTIR

Figure 4 shows the FTIR data of prepared catalysts. The results revealed that the SiO_2 spectra are dominated by three distinct absorption bands originating from Si–O–Si vibrations at 450–1500 cm^{-1}. It can be seen that as Cu–W metals are impregnated with SiO_2, the intensity of the vibration bands at 450–1500 decreases due to the lower silica content compared to the parent silica, accompanied by a down-shift of Si–O–Si bands to a lower wavenumber, indicating a stronger interaction between Cu–W and SiO_2, preferentially generating Si–O–W and Si–O–Cu linkages. The Si–OH bond is responsible for the band at 952 cm^{-1}, while the remainder is caused by structural deformation within the silica network and non-stoichiometric silicon oxide. The existence of bands originating mostly from CH_2 and OH modes due to the presence of organic carbon, as well as bands centered in the 600–700 cm^{-1} range related to the Cu–O stretching vibration, was shown by FTIR data for CW samples.

3.5 UV–Visible Reflectance

As shown in Fig. 5 there is a small beak in the UV wavelength range at 230 nm and there is a sharp variation in the visible wavelength range at 550 nm for SiO_2. There is a wide hump in the wavelength range from 450 to 600 nm at the sample $CW_{(5)}/SiO_2$, at 450 nm for sample $CW_{(15)}/SiO_2$ and there is no variation for the sample $CW_{(25)}/SiO_2$. The direct band-gap is calculated according to the Kubelka–Munk function equation by plotting the square F(R) hυ versus hυ and by the tangent that intercepts the x-axis gives the band-gap. The SiO_2 sample gives 3.9 eV and there is an increase in bandgap in the sample $CW_{(25)}/SiO_2$ to 4.5 EV, but in the samples $CW_{(15)}/SiO_2$ and $CW_{(5)}/SiO_2$ there is a decrease in bandgap to 3.5 EV and 2.5 eV respectively. From the UV–visible reflectance spectra and the calculated bandgap results, we can conclude that the sample $CW_{(5)}/SiO_2$ is the most active in the visible range.

3.6 PL

Photoluminescence spectroscopy is used to identify the electronic structure of molecules. Where, the intensity of the emission spectra reflects the energy difference between the energy levels and the electronic transition between energy levels, which are unique to each molecule. The photoluminescence of the prepared samples at room temperature was presented in Fig. 6 with an excitation

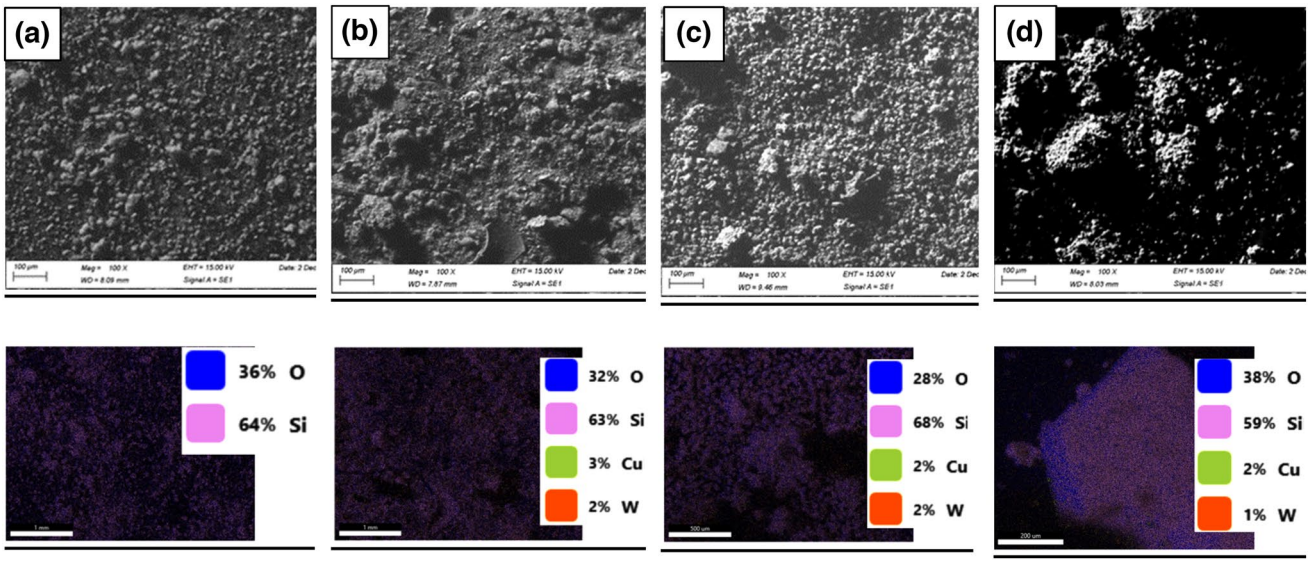

Fig. 7 SEM and SEM–EDS elemental mapping of: **a** SiO_2, **b** $CW_{(5)}/SiO_2$, **c** $CW_{(15)}/SiO_2$ and **d** $CW_{(25)}/SiO_2$

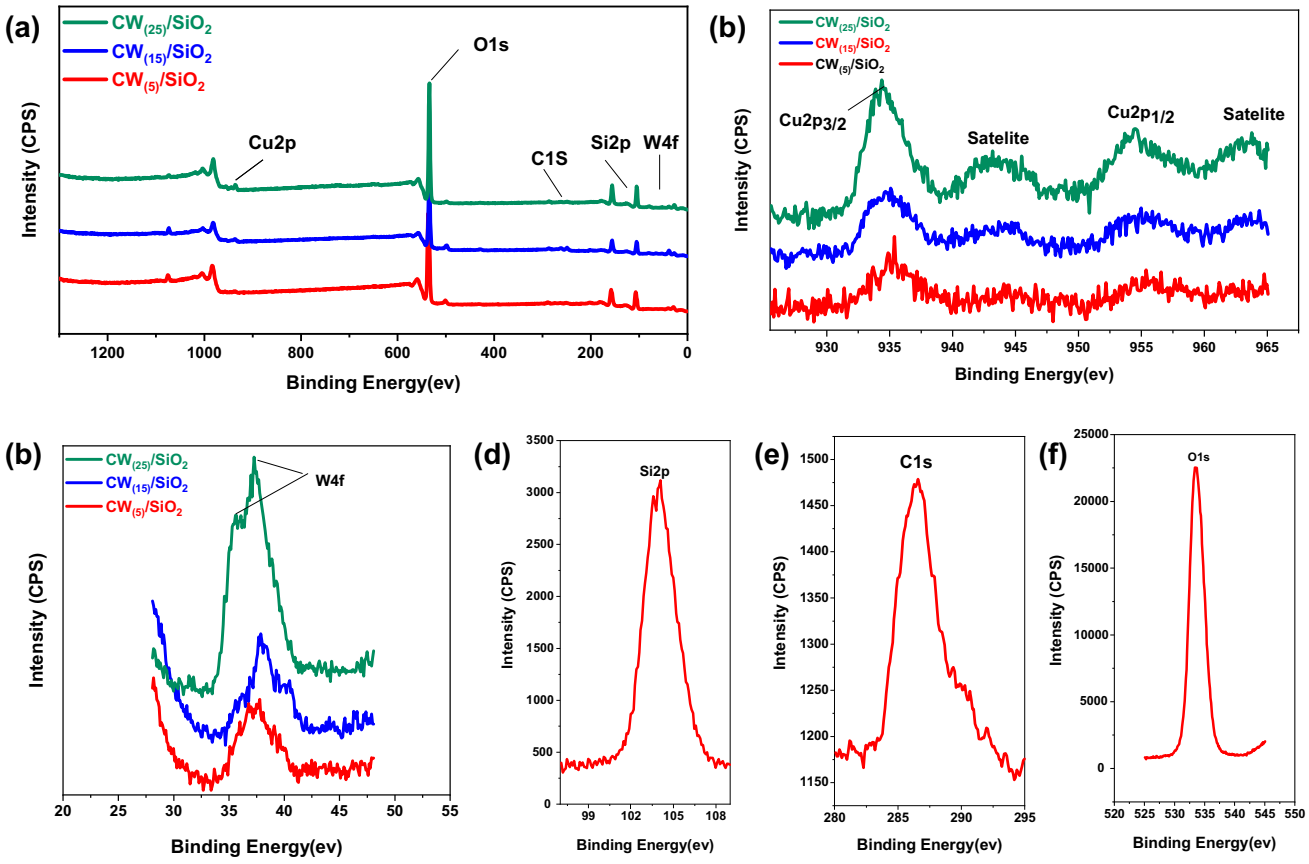

Fig. 8 XPS spectra of impregnated samples **a** Wide scan, and high-resolution scan **b** Cu2p, **c** W4f, **d** Si2p, **e** C1s, **f** O1s

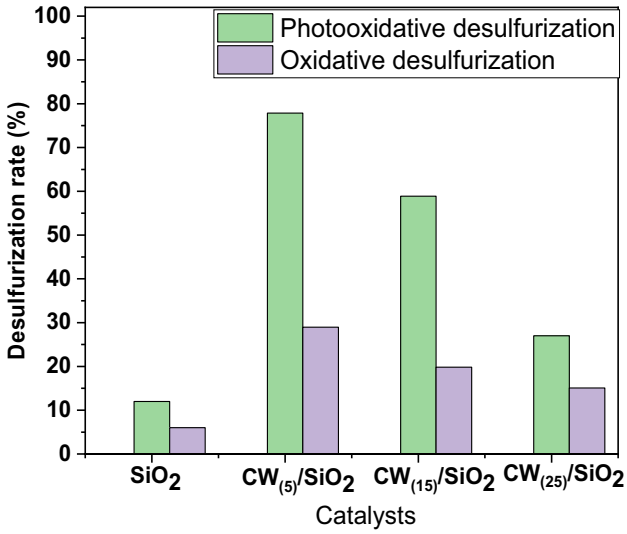

Fig. 9 Effect of different catalysts on DBT removal with or without irradiation. Experimental conditions: V(DBT) = 10 mL (500 ppm), Cat. = 0.03 g, V(H_2O_2) = 2 mL, t = 60 min

wavelength λ = 250 nm. As we show the PL intensity for $CW_{(5)}/SiO_2$ is lower than the other prepared samples which means the recombination of h^+ and e^- is lower and the catalytic activity is better.

3.7 SEM

The morphology of the prepared samples was investigated using scanning electron microscopy (SEM). Also, the elemental mapping (SEM/EDS) was performed for silica before and after the impregnation in Fig. 7. SEM gives the rock-like morphology for all the prepared samples. The percent of Cu and W are very small on the surface as shown in mapping which means the most percent of metals inside the pores are not on the surface. And that is confirmed by the results of surface area and porosity.

3.8 XPS

XPS analysis was performed to verify the presence of Cu, W, Si, and O components in synthesized samples. The survey spectrum of all prepared samples is shown in Fig. 8a. High-resolution XPS spectra of Cu, Si, and O components in $CW_{(5)}/SiO_2$ are displayed in Figs. 8b, c, d, and e, respectively. The XPS results of Cu 2p for $CW_{(5)}/SiO_2$, shown in Fig. 8b, exhibited two main peaks of Cu $2p_{3/2}$ 933.6 eV and Cu $2p_{1/2}$ 953.7 eV, which is consistent with the CuO standard spectrum [30]. However, for $CW_{(15)}/SiO_2$ and $CW_{(25)}/SiO_2$, The Cu 2p spectrum exhibits two main peaks and two satellite peaks, indicating that the spectra were formed by a mixture of Cu^+ and Cu^{2+} ions [31]. Figure 8c depicts the XPS area of W(4f) obtained on $CW_{(5)}/SiO_2$ sample. In this sample, two peaks were detected at 37.1 and 35.2 eV, matching the binding energies of W $4f_{5/2}$ and W$4f_{7/2}$ [32], respectively. This means that the inserted tungsten species have an oxidation state of + 6. The Si 2p spectra revealed two distinguishable peaks located at 103.6, and 104.4 eV on the binding energy spectrum Fig. 8d. These positions are consistent with the known binding energy values for Si^{+2}, and Si^{+3} bonds [33]. The XPS spectra of C 1 s show well-defined maxima at 286 eV Fig. 8e, related carbon covalently bonded to oxygen(C=O) [34]. Figure 8f depicts the O1s spectrum. It has a peak at 533.5 eV that is connected to C=O bonds [35].

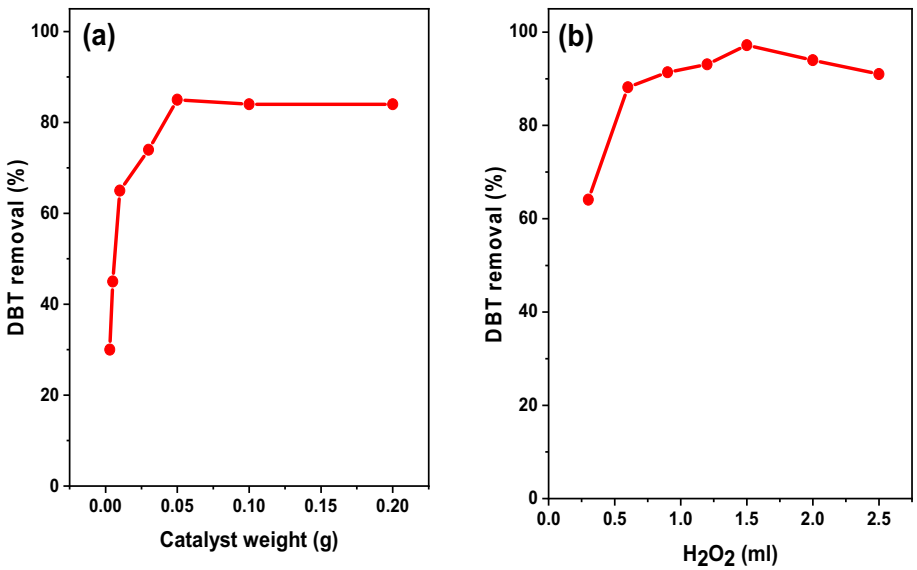

Fig. 10 Effect of **a** catalyst dosses, and **b** oxidant dose on ODS of dibenzothiophene over $CW_{(5)}/SiO_2$. Experiment conditions: V(DBT) = 10 mL (500 ppm). **a** V(H_2O_2) = 2 mL; t = 60 min. **b** cat = 0.05 g

4 Photocatalytic Activity

4.1 Effect of Different Catalysts on Sulfur Removal with and Without Irradiation

Desulfurization of DBT with different prepared catalysts for photocatalytic oxidation with irradiation or without as shown in Fig. 9. It shows that the sulfur removal of the system with irradiation was higher than the system without. These results confirmed that solar light is essential for the removal of DBT. Without irradiation, a catalyst can react with H_2O_2 to generate peroxo-species to oxidize DBT. While the irradiation process, conduction band electrons (e) and valence band holes (h+) were formed. The (e) would react with the H_2O_2 to give hydroxyl radicals (HO·), which could then oxidize DBT to the corresponding sulfones [36]. Heterojunction formation between two metal oxides inhibited photogenerated electron–hole pair recombination, resulting in more photogenerated carriers being generated for PODS due to the rapid transport of photoexcited electron–hole pairs at the heterojunction's interface, greatly improving activity [37, 38]. Therefore, the heterojunction of CuW-supported catalysts has much higher activities than pure support. The $CW_{(5)}/SiO_2$ has the highest desulfurization rate was approximately 77.84% within 60 min of visible light irradiation. The high activity of $CW_{(5)}/SiO_2$ might be attributed to the ability of $CW_{(5)}/SiO_2$ to provide sufficient active sites and sufficient activity for the PODs reaction. However, The $CW_{(15)}/SiO_2$ and $CW_{(25)}/SiO_2$ photocatalyst have a lower desulfurization rate than the $CW_{(5)}/SiO_2$. Since the particles agglomerated at higher total metal loadings (greater than 5% wt.%), the surface area available for the photooxidation process was reduced. As a result, $CW_{(5)}/SiO_2$ was chosen to optimize the photocatalytic oxidation process.

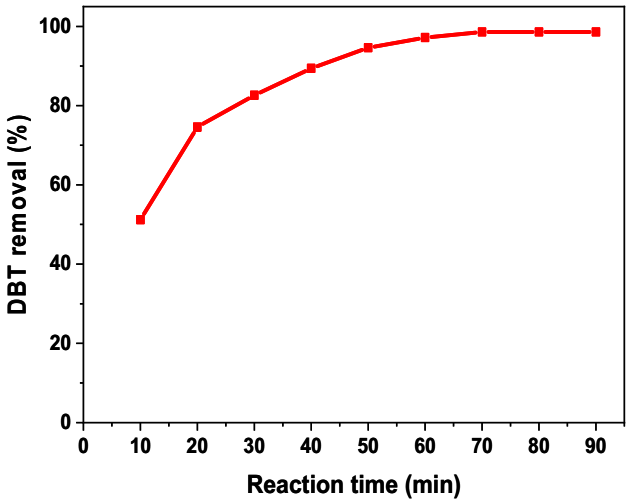

Fig. 11 Effect of reaction time on ODS of dibenzothiophene over $CW_{(5)}/SiO_2$. Experiment conditions: V(DBT) = 10 mL (500 ppm); cat = 0.05 g; Oxidant dose (30 wt.%) = 1.5 mL

4.2 The Effect of Various Parameters on DBT Removal

As illustrated in Fig. 10, The catalyst dose, and Oxidant volume, were optimized. Figure 10a shows the effect of catalyst dose on photocatalytic DBT removal. The % DBT removal increased with an increase in catalyst weight from 0.003 to 0.05 g and the decrease slows down at 0.1 g. The increase in activity with increasing catalyst dosage is attributed to an increase in the number of active sites for light absorption. But at 0.1 g Catalyst dose, there is a hindrance in light penetration to reaching the active catalyst surface and the reactant [39]. As a result, 0.05 g was selected as the optimum amount of catalyst weight. Figure 10b displays the relationship between the DBT removal and the H_2O_2 doses. It can be observed that when the H_2O_2 dose rises, the desulfurization rate initially increases and subsequently falls. As well as excessive hydrogen peroxide can cause H_2O molecules to occupy the active sites, resulting in decreased DBT adsorption by the catalyst and a subsequent drop in the DBT removal [21, 23, 40] DBT is almost completely removed at H_2O_2 = 1.5 mL for DBT removal 97.2%. In sum, the optimum conditions for this study are catalyst dose = 0.05 g/10 mL, and Oxidant dose of 1.5 mL that was used for further studies.

4.3 The Effect of Reaction Time on DBT Removal

Figure 11a displays the effect of reaction time on DBT removal using $CW_{(5)}/SiO_2$. DBT has almost completely removed 98.6% removal at 70 min. Further prolonging the reaction time to 90 min, there is no significant increase in catalytic activity. Therefore, 70 min is considered to be the optimum reaction time in the present study.

Table 2 The pseudo first-order and pseudo-second order parameters for photooxidative DBT over $CW_{(5)}/SiO_2$

Pseudo first order				Pseudo second order			
K_1	qe_{calc}	qe_{exp}	R^2	K_2	qe_{calc}	qe_{exp}	R^2
0.02112	18.5	20	0.98	0.001751	23	20	0.97

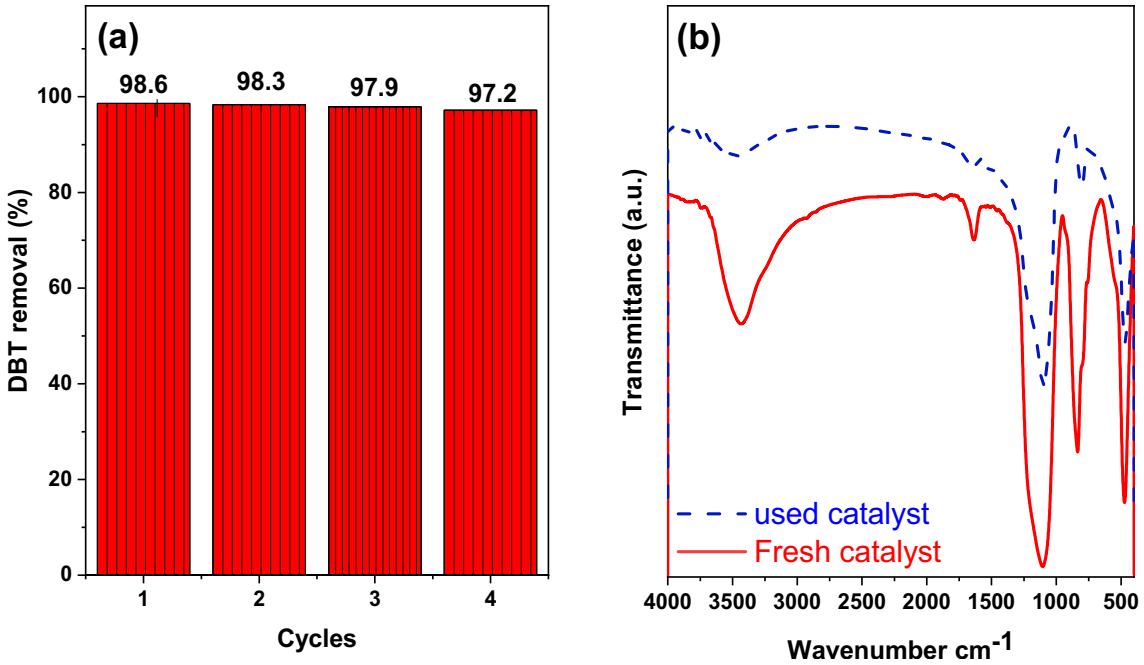

Fig. 12 Effect of **a** recycling of the PODS of dibenzothiophene over $CW_{(5)}$ /SiO_2. Experiment conditions: V(DBT) = 10 mL (500 ppm); cat = 0.05 g; Oxidant dose (30 wt.%) = 1.5 mL; time = 70 min. **b** FT-IR of fresh $CW_{(5)}/SiO_2$ and after PODS reaction

Table 3 The comparison of $CW_{(5)}$ /SiO_2catalyst with other published research work in the PODS process of DBT

Photocatalyst	Sulfur removal (%)	Catalyst dose (gm/L)	Irradiation time	Temp	References
Ag@AgBr/Al-SBA-15	98.66	2	360	70	[41]
Ti–Al-SBA-15	92.68%	2	360	–	[42]
Nb_2O_5/Bi_2WO_6	99	7.5	120	Ambient temp	[37]
Ag-AgBr/Al-MCM-41	99.2	2.5	360	70	[43]
MoS_2-CeO_2/SiO_2-Al_2O_3 PEG	98	4	60	25	[44]
CeF_3/g-C_3N_4	84.2	0.5	180	–	[45]
CeO_2/MIL-101(Fe)	90	1	120	–	[46]
0.2% $CuWO_4/WO_3$	85	10	120		[47]
TiO_2/g-C_3N_4	98.9	10	120	30	[48]
$CW_{(5)}$ /SiO_2	98.6	1	70	Ambient temp	This study

4.3.1 Reaction Kinetics

We studied the kinetics of the photo-oxidative desulfurization of DBT as model sulfur compound over $CW_{(5)}SiO_2$ and the kinetic data were analyzed using two models: pseudo-first order and pseudo-second-order.

Pseudo first order:

$$Ln\left(q_e - q_t\right) = Lnq_e - K_1 t \tag{1}$$

Pseudo second order:

$$\frac{t}{q_t} = \frac{1}{K_2 q_{e^2}} + \frac{1}{qe} t \tag{2}$$

where, q_e (mg/gm): the adsorption capacity at equilibrium. q_t (mg/gm): the adsorption capacity at time t (min). K_1:(min^{-1}): the pseudo first order rate constant. K_2:(gm/mg.min): the pseudo second order rate constant. t (min): is the illumination duration.

when we plot Ln(q_e−q_t) versus time in Eq. (1) we can obtain K_1 from the slope and q_e from the intercept. Where, when we applied the pseudo second order model we plot t/q_t versus time t and we can obtain q_e from slope and K_2 from intercept as shown in Table 2. By comparing the value of q_e

calculated and q_e experimental in case of pseudo first order and pseudo second order model we can concluded that; the photooxidative of DBT over CW/SiO_2 is pseudo first order reaction.

4.4 The Effect of Recycling Times on DBT Sulfur Removal Over $CW_{(5)}/SiO_2$

The stability of $CW_{(5)}/SiO_2$ was studied by testing sequential cycles of the photocatalytic process, as illustrated in Fig. 12. After the PODS reaction, the catalyst was filtered, dried at 80 °C, and exposed to the next run. The results show that, after the 4th cycle, the DBT removal remains above 97%. In sum, the catalyst shows no significant loss of activity, which indicates excellent photocatalytic stability. In addition, Fig. 12b shows the IR patterns of the $CW_{(5)}/SiO_2$ before and after PODS. It showed that the used $CW_{(5)}/SiO_2$ had a comparable IR to the fresh one, with the exception that the peak strength was somewhat lower.

4.5 Photocatalytic Performance in Comparison to Other Photocatalysts

A comparison study on the photo-oxidative desulfurization of DBT over different catalysts using H_2O_2 as an oxidant was presented in Table 3 [37, 41–48]. It is obvious that the $CW_{(5)/}SiO_2$ is comparable with other catalysts stated in the literature. As seen through this Table, the synthesized catalyst in the current study exhibited a very good catalytic performance for the DBT's sulfur removal from a model fuel according to operating criteria. In other words, the prepared catalyst in this study held a very high and comparably good DBT sulfur removal (of 98.6%) utilizing the lowest catalyst dose (1 g/L) at ambient temperature. Ag-AgBr/Al-MCM-41 and Nb_2O_5/Bi_2WO_6 catalysts showed a higher removal rate for a longer time 360 and 120 min with the higher catalyst dose of 2.5 and 7.5 gm/L could contribute to the higher cost. As a consequence, this research is extremely advantageous for fuel treatment, and it has the potential to significantly lower processing costs.

5 Conclusion

The photocatalytic ODS of model oil was investigated over CW-supported SiO_2, with hydrogen peroxide as the oxidant. The catalysts were synthesized and thoroughly characterized using a variety of techniques. The research revealed that the $CW_{(5)}/SiO_2$ composite has the highest sulfur removal of model oil and has an efficiency of 98.2 percent under optimal conditions (catalyst dosage = 0.05 g/10 mL, oxidant dose 1.5 mL, and 70 min). The pseudo-first-order kinetic model for catalytic ODS was determined. According to the current study, simplicity of operation, low cost, raw material availability, operation in moderate conditions, and high efficiency may be employed as a catalyst in PODS on an industrial scale.

Funding Open access funding provided by The Science, Technology & Innovation Funding Authority (STDF) in cooperation with The Egyptian Knowledge Bank (EKB).

References

1. J.M. Campos-Martin, M.C. Capel-Sanchez, J.L.G. Fierro, Green Chem. **6**, 557 (2004)
2. A. Stanislaus, A. Marafi, M.S. Rana, Catal. Today **153**, 1 (2010)
3. H. Zheng, Z. Sun, X. Chen, Q. Zhao, X. Wang, Z. Jiang, Appl. Catal. A Gen. **467**, 26 (2013)
4. X. Zeng, X. Xiao, Y. Li, J. Chen, H. Wang, Appl. Catal. B Environ. **209**, 98 (2017)
5. N.F. Nejad, E. Shams, M.K. Amini, J.C. Bennett, Fuel Process. Technol. **106**, 376 (2013)
6. W.S. Ahmed Rahma, F.S. Mjalli, T. Al-Wahaibi, A.A. Al-Hashmi, Chem. Eng. Res. Des. **120**, 271 (2017)
7. T. Optenhostert, S. Puthenkalam, N. Stegmann, M. Steffen, W. Schmidt, Chem.-Ing.-Tech. **93**, 1028 (2021)
8. F. Yu, C. Liu, B. Yuan, P. Xie, C. Xie, S. Yu, Fuel **177**, 39 (2016)
9. D.M. Abd El-Aty, O.I. Sif El-Din, S.I. Hassan, S.M. Tawfik, S. Hanafi, Pet. Sci. Technol. **27**, 861 (2009)
10. D.M. Abd El-Aty, T. Zaki, S.M. Tawfik, O.I.S. El-Dine, S.I. Hassan, S.H. Ahmed, Egypt. J. Chem. **59**, 381 (2016)
11. K.X. Lee, J.A. Valla, React. Chem. Eng. **4**, 1357 (2019)
12. S.I. Hassan, O.I.S. El-Din, S.M. Tawfik, D.M. Abd El-Aty, Fuel Process. Technol. **106**, 127 (2013)
13. M.A. Rezvani, M.A. Asli, S. Khandan, H. Mousavi, Z.S. Aghbolagh, Chem. Eng. J. **312**, 243 (2017)
14. F. Lin, Z. Jiang, N. Tang, C. Zhang, T. Liu, B. Dong, Appl. Catal. B Environ. **188**, 253 (2016)
15. L. Yun, Z. Yang, Z.-B. Yu, T. Cai, Y. Li, C. Guo, C. Qi, T. Ren, RSC Adv. **7**, 25455 (2017)
16. I. Shafiq, M. Hussain, S. Shafique, R. Rashid, P. Akhter, A. Ahmed, J.-K. Jeon, Y.-K. Park, J. Ind. Eng. Chem. **98**, 283 (2021)
17. Y. Zhu, X. Li, M. Zhu, Catal. Commun. **85**, 5 (2016)
18. C.-J. Jia, L.-D. Sun, L.-P. You, X.-C. Jiang, F. Luo, Y.-C. Pang, C.-H. Yan, J. Phys. Chem. B **109**, 3284 (2005)
19. M. Mousavi-Kamazani, S. Ashrafi, Ultrason. Sonochem. **63**, 104948 (2020)
20. I. Shafiq, M. Hussain, N. Shehzad, I.M. Maafa, P. Akhter, S. Shafique, A. Razzaq, W. Yang, M. Tahir, N. Russo, J. Environ. Chem. Eng. **7**, 103265 (2019)
21. B. Wang, B. Dai, L. Kang, M. Zhu, Fuel **265**, 117029 (2020)

22. H.F. Mohd Zaid, F.K. Chong, M.I. Abdul Mutalib, Fuel **156**, 54 (2015)
23. B. Wang, B. Dai, M. Zhu, ACS Omega **5**, 378 (2020)
24. H.M. Salem, R.S. Mohamed, A.A. Alkahlawy, H.M. Gobara, A.E.A. Hassan, S.A. Hassan, J. Porous Mater. **26**, 735 (2019)
25. A. Nakajima, T. Kobayashi, T. Isobe, S. Matsushita, Mater. Lett. **65**, 3051 (2011)
26. H. A. Shamsel-Din, E. G. Zaki, J. Radioanal. Nucl. Chem. 1 (2020).
27. J. Robertson, T.J. Bandosz, J. Colloid Interface Sci. **299**, 125 (2006)
28. M. Zarrabi, M.H. Entezari, E.K. Goharshadi, Rsc Adv. **5**, 34652 (2015)
29. K.S.W. Sing, R.T. Williams, Adsorpt. Sci. Technol. **22**, 773 (2004)
30. A.T. Le, S.-Y. Pung, S. Sreekantan, A. Matsuda, Heliyon **5**, e01440 (2019)
31. K. Munawar, M.A. Mansoor, W.J. Basirun, M. Misran, N.M. Huang, M. Mazhar, RSC Adv. **7**, 15885 (2017)
32. P. Wang, P.-S. Yap, T.-T. Lim, Appl. Catal. A Gen. **399**, 252 (2011)
33. G. Zheng, Y. Xiang, L. Xu, H. Luo, B. Wang, Y. Liu, X. Han, W. Zhao, S. Chen, H. Chen, Adv. Energy Mater. **8**, 1801718 (2018)
34. P.V. Krasovskii, O.S. Malinovskaya, A.V. Samokhin, Y.V. Blagoveshchenskiy, V.A. Kazakov, A.A. Ashmarin, Appl. Surf. Sci. **339**, 46 (2015)
35. A. Roy, A.K. Mukhopadhyay, S.C. Das, G. Bhattacharjee, A. Majumdar, R. Hippler, Coatings **9**, 551 (2019)
36. W. Zhu, Y. Xu, H. Li, B. Dai, H. Xu, C. Wang, Y. Chao, H. Liu, **31**, 211 (2014).
37. J. Wu, J. Li, J. Liu, J. Bai, L. Yang, RSC Adv. **7**, 51046 (2017)
38. S. Li, S. Hu, W. Jiang, Y. Liu, J. Liu, Z. Wang, J. Colloid Interface Sci. **501**, 156 (2017)
39. S. Khayyat, L.S. Roselin, J. Saudi Chem. Soc. **21**, 349 (2017)
40. H.F.M. Zaid, F.K. Chong, M.I.A. Mutalib, Fuel **156**, 54 (2015)
41. X.N. Pham, M.B. Nguyen, H.S. Ngo, H.V. Doan, J. Ind. Eng. Chem. **90**, 358 (2020)
42. X.N. Pham, M.B. Nguyen, H.V. Doan, Adv. Powder Technol. **31**, 3351 (2020)
43. X.N. Pham, B.M. Nguyen, H.T. Thi, H. Van Doan, Adv. Powder Technol. **29**, 1827 (2018)
44. S. Mohammadzadeh Yengejeh, S. Allahyari, N. Rahemi, Process Saf. Environ. Prot. **143**, 25 (2020)
45. X. Lu, F. Chen, J. Qian, M. Fu, Q. Jiang, Q. Zhang, J. Rare Earths **39**, 1204 (2021)
46. Q. Huo, G. Liu, H. Sun, Y. Fu, Y. Ning, B. Zhang, X. Zhang, J. Gao, J. Miao, X. Zhang, S. Liu, Chem. Eng. J. **422**, 130036 (2021)
47. M. Kang, X. Wang, J. Zhang, Y. Lu, X. Chen, L. Yang, F. Wang, J. Environ. Chem. Eng. **7**, 102809 (2019)
48. C. Wang, W. Zhu, Y. Xu, H. Xu, M. Zhang, Y. Chao, S. Yin, H. Li, J. Wang, Ceram. Int. **40**, 11627 (2014)

Authors and Affiliations

Heba M. Salem[1] · Dina Mohmed[1] · E. G. Zaki[1]

[1] Egyptian Petroleum Research Institute (EPRI), Nasr City 11727, Cairo, Egypt